Indian Journal of Chemistry
Vol. 64, August 2025, pp. 799-814
DOI: 10.56042/ijc.v64i8.14700

Synthesis and comparison of experimental and theoretical results of N'-(4-(*tert*-butyl)benzylidene)-1-(2-methoxyphenyl)-5-methyl-1*H*-pyrazole-4-carbohydrazide

Şehriman Atalay*[a] & Aliye Gediz Ertürk[b]

[a] Department of Physics, Faculty of Science and Arts, Ondokuz Mayıs University, 55200 - Atakum - Samsun, Turkey

[b] Department of Chemistry, Faculty of Science and Arts, Ordu University, 52200 Ordu, Turkey

E-mail: atalays@omu.edu.tr

Received 29 October 2024; accepted (revised) 30 July 2025

N'-(4-(*tert*-Butyl)benzylidene)-1-(2-methoxyphenyl)-5-methyl-1*H*-pyrazole-4-carbohydrazide **3**, has been successfully obtained from substituted N-acyl hydrazide **1** and 4-*tert*-butyl benzaldehyde **2** *via* condensation reaction and subsequently purified. X-ray crystal structures of the synthesized compound **3** have been determined. The molecular structure of the compound has been further elucidated by FT-IR, ^{1}H and APT-^{13}C NMR and LC-MS-QTOF spectroscopic methods. The geometry derived from the X-ray experiments has been compared with theoretical calculations using Hartree-Fock (HF) and density functional theory (DFT) using the 6-31G+(d,p) basis set to validate the experimental results. The results show good agreement between the calculated and experimental structures of the compound. In addition, Molecular Electrostatic Potential (MEP), Frontier Molecular Orbital (FMO), and Hirshfeld surface analyses have been performed to gain further insight into the molecular structure. Thermal analysis and nonlinear optical (NLO) characterization are integral to this comprehensive study.

Keywords: X-ray, Theoretical calculations, Hirshfeld surface analysis, NLO, Thermal analysis

In recent years, hydrazones (–C=N–NH–) are a functional group that has become the focus of attention in chemistry due to both their chemical and biological activities[1]. Hydrazones with azomethine motifs are not only intermediate compounds involved in the synthesis of different rings with heteroatoms, but they are also organic compounds class that have proven themselves with their chemical properties, industrial outputs[2], and especially acyl hydrazone (–C=N–NH–CO–) derivatives[3] that show a wide range of biological activities. In addition to its easy synthesis, its highly stable hydrazone (-C=N-NH-) group, nucleophilic imine nitrogen, and both nucleophilic and electrophilic imine carbon features make it a versatile organic material such as configurational isomerism[4], sensors[5]. In addition, stable complex compounds were formed by using transition metal cations, oxygen, and imine nitrogen in the basic motif structure as donor atoms[6]. The ability of acyl hydrazones to respond to structural, conformational, and configurational dynamics makes them striking candidates for applications in structural dynamics[7]. Therefore, investigating acyl hydrazones with DFT is both useful for understanding these dynamics and provides insight into their different conformational structures and stability[8]. This study, X-ray crystal structures were determined for compound (3), and its molecular structure was further elucidated using FT-IR spectroscopy. Theoretical calculations were performed to validate experimental results, showing good agreement. Additional analyses provided insight into the molecular structure, while thermal and nonlinear optical characterization were crucial components of the study.

Experimental Section

Synthesis of N -(4-(*tert*-butyl)benzylidene)-1-(2-methoxyphenyl)-5-methyl-1*H*-pyrazole-4-carbohydrazide

In ethanol (5 mL), 1-(2-methoxyphenyl)-5-methyl-1*H*-pyrazole-4-carbohydrazide (1) (0.25 mmol, 62.00 mg), 4-*tert*-butyl benzaldehyde (2) (0.25 mmol, 42 mg) and two drops of acetic acid were mixed. It was heated under reflux for 2 hours (Scheme 1). The mixture was evaporated and washed with diethyl ether and cold ethyl alcohol. The resulting solids were crystallized from acetonitrile using the slow evaporation method (Scheme 1). White solid (60 mg, 62%). m.p.196-197°C. R_f: 0.35 (Ethyl

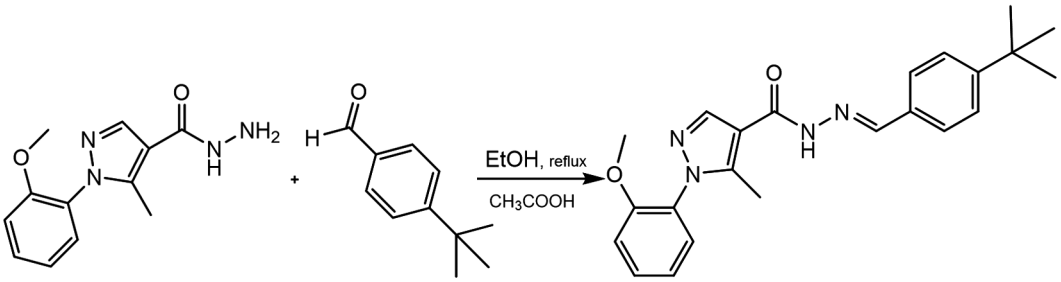

Scheme 1 — Synthesis of the title compound **3**

acetate: Petroleum ether 3:2); FT-IR (ATR): 3201, 3024, 2954, 2831, 1643 C=O, 1604 C=N, 1566 - 1465, C=C, 1273, 1118, 1018, 894, 756 cm^{-1}; ^{1}H NMR (400 MHz, DMSO-d_6): δ 11.45 (s, 1H, NH), 8.37 (s, 1H, N=CH), 8.17 (s, 1H, pyrazole ring = CH), 7.65 (d, *J*: 7.4 Hz 2H, *t*-Bu-benzaldehyde ring =CH), 7.55 (t, *J*: 7.9 Hz, 1H, 2-methoxyphenyl =CH), 7.49 (d, *J*: 8.4 Hz 2H, *t*-Bu-benzaldehyde ring =CH), 7.36 (d, *J*: 7.7 Hz, 1H, 2-methoxyphenyl =CH), 7.28 (d, *J*: 8.1 Hz, 1H, 2-methoxyphenyl =CH), 7.12 (t, *J*: 7.5 Hz, 1H, 2-methoxyphenyl =CH), 3.80 (s, 3H, 2-methoxyphenyl -OCH_3), 2.30 (s, 3H, pyrazole ring -CH_3), 1.31 (s, 9H, -$C(CH_3)_3$); APT-^{13}C NMR (100 MHz, DMSO-d_6): δ 159.84, 154.54, 153.15, 147.29, 146.60, 139.07, 132.31, 131.47 (2C), 129.27, 127.51, 127.22 (2C), 126.12, 121.21, 113.54, 113.07, 56.22, 35.08, 31.11 (3C), 11.17; LC/MS-TOF: Calcd for $C_{23}H_{26}N_4O_2$: *m/z* $(M + H)^+$ = 391.2126. Found $(M + H)^+$ = 391.2141.

X-ray crystallographic study

Table 1 provides an exhaustive account of the procedures implemented for the meticulous collection, analysis, and refinement of data about the compound (3). Intensity data were acquired at a temperature of 293(2) K, employing monochromatic MoKα radiation (λ=0.71073Å). The experiments were conducted using a STOE IPDSII diffractometer equipped with a graphite crystal monochromator. The determination of the molecular structure was orchestrated through the synergistic utilization of SHELXS97 (Ref. 9) and direct methods. Subsequent refinement on F2 was executed through full-matrix least squares, incorporating anisotropic thermal parameters for all atoms, excluding hydrogen atoms. This refinement process was facilitated by the SHELXL2014 software[10].

Positioning of hydrogen atoms was achieved through calculated coordinates grounded in geometric considerations, where C-H distances ranged from 0.93 to 0.96Å. The refinement of hydrogen atoms followed the Riding model, adopting Uiso(H)=1.2Ueq(C) for all atoms, except ethyl and methyl groups, where Uiso(C)=1.5Ueq(C) was applied. It's important to note that the slightly elevated R and wR2 values observed in the results may be attributed to factors such as the suboptimal crystal quality, limited crystal dimensions, and the presence of crystal

Table 1 — Crystallographic data for **3**

Crystal data	
Chemical formula	$C_{23}H_{26}N_4O_2$
M_r	390.48
Crystal system, space group	Orthorhombic, $P2_12_12_1$
Crystal shape/color	Prism/Colorless
Temperature (K)	293
a, *b*, *c* (Å)	8.4978 (8), 14.4687 (17), 17.788 (2)
V (Å^3)	2187.1 (4)
Z	4
D_x(Mg cm^{-3})	1.186
F_{000}	832
Radiation type	Mo K_α
μ (mm^{-1})	0.08
Crystal size (mm)	0.67, 0.11, 0.06
Data collection	
Diffractometer	STOE IPDS 2
Absorption correction	0.9902, 0.9579
No. of measured, independent and observed [$I > 2\sigma(I)$] reflections	9566, 3872, 1535
R_{int}	0.135
θ_{max}, θ_{min}	25.1°, 1.8°
Refinement	
$R[F^2 > 2\sigma(F^2)]$, $wR(F^2)$, *S*	0.090, 0.264, 0.91
No. of reflections	3872
No. of parameters	266
$\Delta\rho_{max}$, $\Delta\rho_{min}$ (e Å^{-3})	0.44, −0.25
Programs	Wingx, PLATON (Ref. 11,12)
CCDC	2321709

defects, underscoring the need for cautious interpretation.

Results and Discussion

Vibration analysis

The structure of the synthesized target compound (**3**) was detected by the FT - IR method (Fig. 1). In the infrared spectrum taken with the ATR accessory for compound (**3**), it was observed that the severe bidentate peak belonging to the amino (-NH_2) end of carbohydrazide 1 disappeared, and a monodentate - NH peak appeared at 3201 cm^{-1} (Fig. 1). In addition the carbohydrazide carbonyl (C=O) peak was observed at 1643 cm^{-1}. A sign that strongly confirms the formation of compound (**3**) is the new peak observed at 1604 cm^{-1} of the imine (-N=CH) bond in the product[13]. The peaks at 894 and 756 cm^{-1} are the bending peaks of *p* - *p*-disubstituted benzene, which occur when the imine and *tert*-butyl groups are placed in the *para* position relative to each other (Table 2).

NMR and Mass Spectral Analysis

The key player in the NMR spectrum for confirming the synthesis of the desired compound is the peak corresponding to azomethine (HC=N). Therefore, it was evaluated that the azomethine peak appeared at 8.37 ppm, the carbahydrazide (-NH) proton at 11.45 ppm, the methoxy protons at 3.80 ppm, and the *tert*-butyl protons at 1.31 ppm[14]. When we look at the counterparts of the same determinant groups in APT-carbon 13 NMR, we observe the following peaks: the azomethine (HC=N) carbon peak at 146.60 ppm, the carbahydrazide carbonyl (C=O) carbon peak at 159.84 ppm, the methoxy (-OCH_3) carbon peak at 56.22 ppm, and the *tert*-butyl carbon peak at 35.08 ppm[15]. Another finding that bolsters our argument in the characterization of compound (**3**) through spectroscopy is the remarkable correlation between the calculated $(M + H)^+$ and detected $(M + H)^+$ values in the mass spectrum. The calculated $(M + H)^+$ value for the molecule represented by the formula $C_{23}H_{26}N_4O_2$ is 391.2126, whereas the found $(M + H)^+$ value is 391.2141 (Fig. 2, Fig. 3, Fig. 4).

X-ray analysis

Fig. 5 meticulously illustrates the Ortep diagram, providing an in-depth visualization of the intricate molecular structure of the compound (3). Complementing this, Fig. 6 extends our comprehension by offering detailed packing diagrams that elucidate intermolecular interactions and bonding configurations. For a comprehensive exploration, Table 1 collates a wealth of geometric parameters, spanning hydrogen bonding specifics, crystal parameters, and pertinent details on data collection and purification.

Table 2 — Some selected experimental and theoretical vibrational bands of **(3)** (cm^{-1})

Vibrations	Experimental	DFT
ν (N–H) ring	3201	3327
ν (N–H)	3024	3117
ν (C–H)	2954–2831	3098–2892
ν (C=O)	1643	1543
ν (C=N)	1604	1580
ν (C=C)	1566–1465	1496, 1480
γ (N–H)	1273	1261
ω (C–H)	756	728

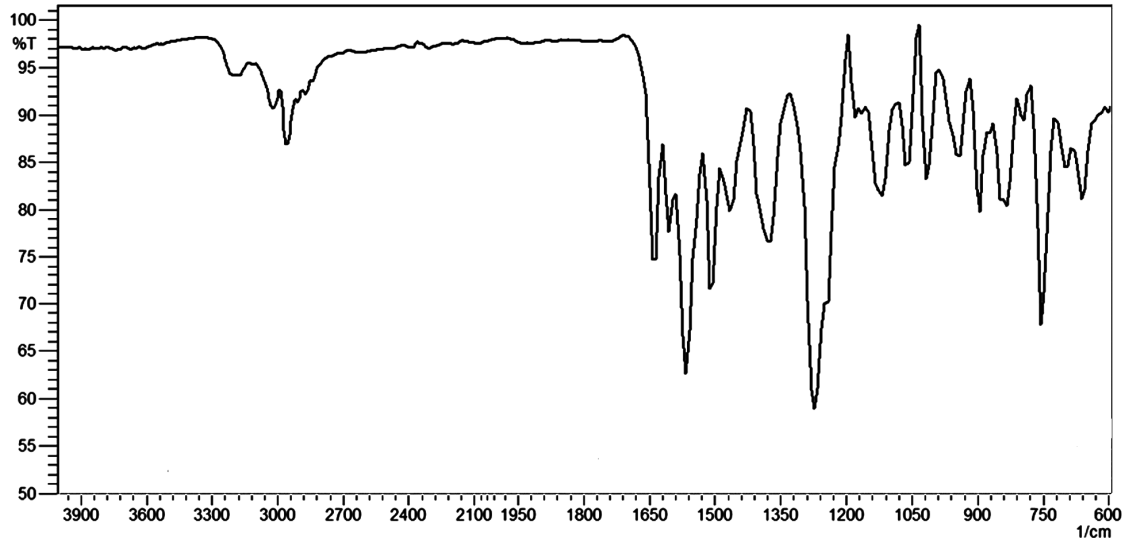

Fig. 1 — FT-IR spectrum of **3**

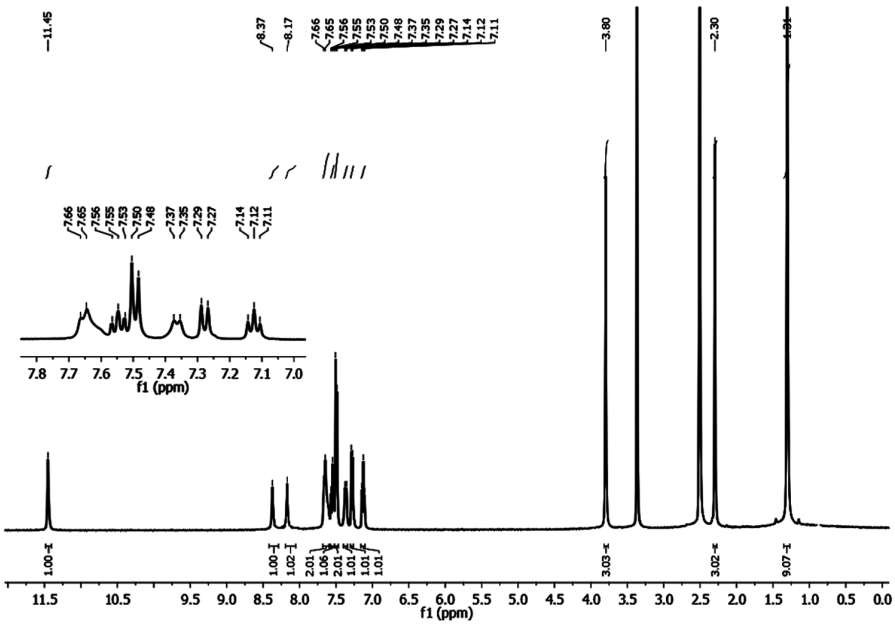

Fig. 2 — ^{1}H NMR spectrum of **3**

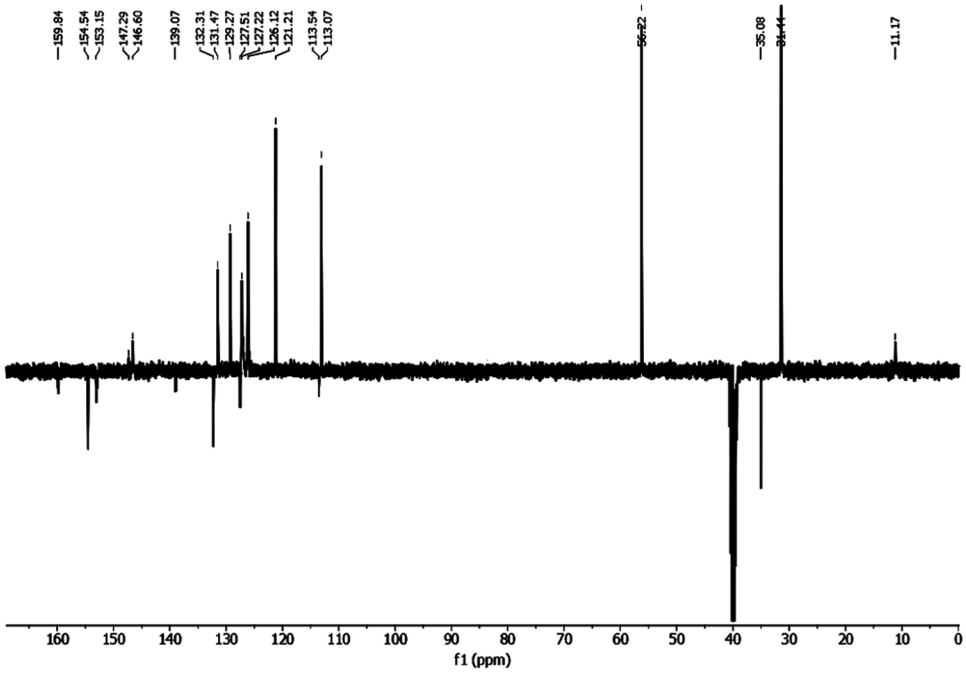

Fig. 3 — APT ^{13}C NMR spectrum of **3**

Diving into the structural nuances of compound (3), its distinctive non-planar configuration unfolds, marked by a notable dihedral angle of 82.96° between the C5/C10 and C17/C22 aromatic rings. The crystal structure aligns with the $P2_12_12_1$ space group, with the unit cell accommodating two molecules, as visually represented in the packing diagram. The stability of molecule (3) is underpinned by a network of intermolecular hydrogen bonds, encompassing C-H···N, N-H···N, and C-H···O types, detailed comprehensively in Table 3. Significantly, specific bond lengths stand out, such as C11=N1 [1.264 (11) Å], N1 - N2 [1.416 (9) Å], C12=O1 [1.202 (10) Å], and C22 - O2 [1.377 (11) Å]. These observations echo findings from analogous studies on hydrazones[16]. To enrich our exploration, Table 4 amalgamates selected

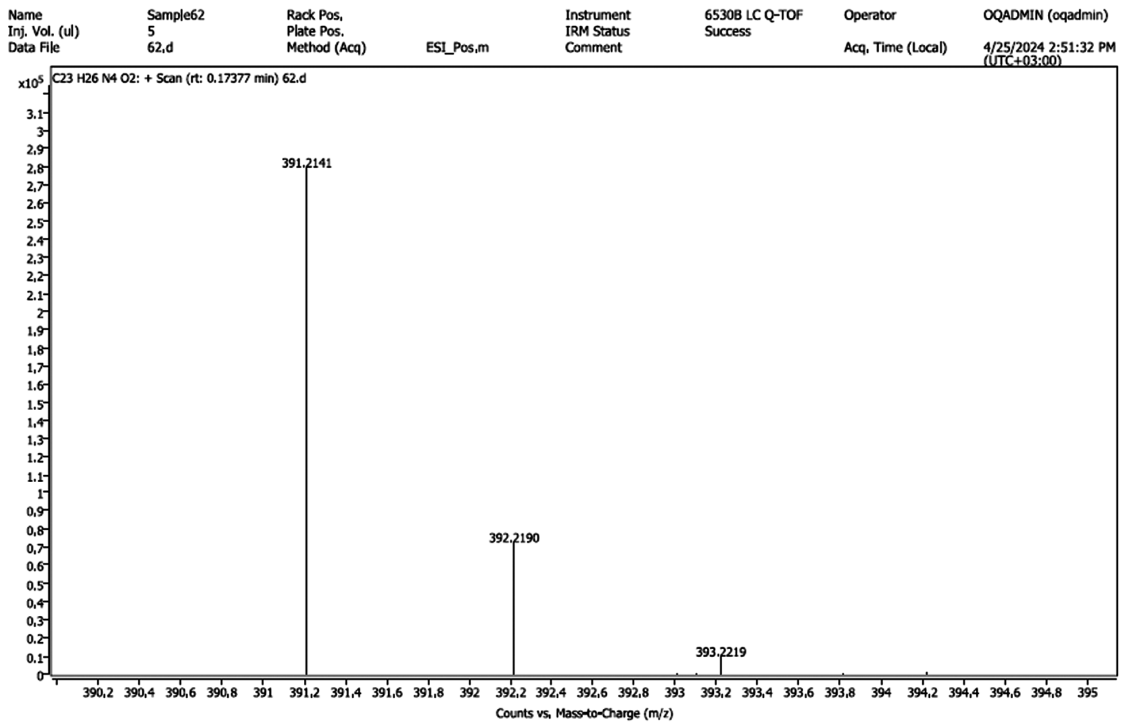

Fig. 4 — LC/MS-QTOF spectrum of **3**

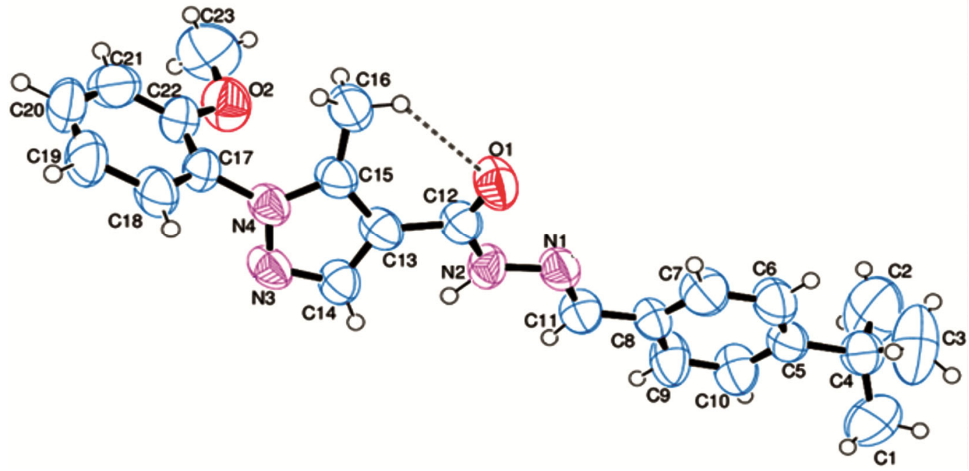

Fig. 5 — Ortep diagram of **3**

bond lengths, bond angles, and torsion angles for (3), offering a holistic perspective on its structural intricacies.

Computational studies

The exploration of compound (3) involved a meticulous geometric optimization process employing both the DFT with B3LYP functional (DFT/B3LYP) and HF methods under the umbrella of a 6-31G+(d,p) basis set. The Gaussian03 (Ref. 17) and Gaussview4.1 (Ref. 18) software platforms were instrumental in orchestrating these intricate theoretical calculations. An exhaustive examination of molecular atomic parameters was conducted within the Gaussian03 program before initiating the calculations to fortify the theoretical foundations.

A rigorous comparative analysis was then undertaken, delving into and contrasting the optimized geometric parameters derived from both the DFT/B3LYP and HF methods. This scrutiny aimed to discern nuances and disparities between the two approaches, providing a comprehensive

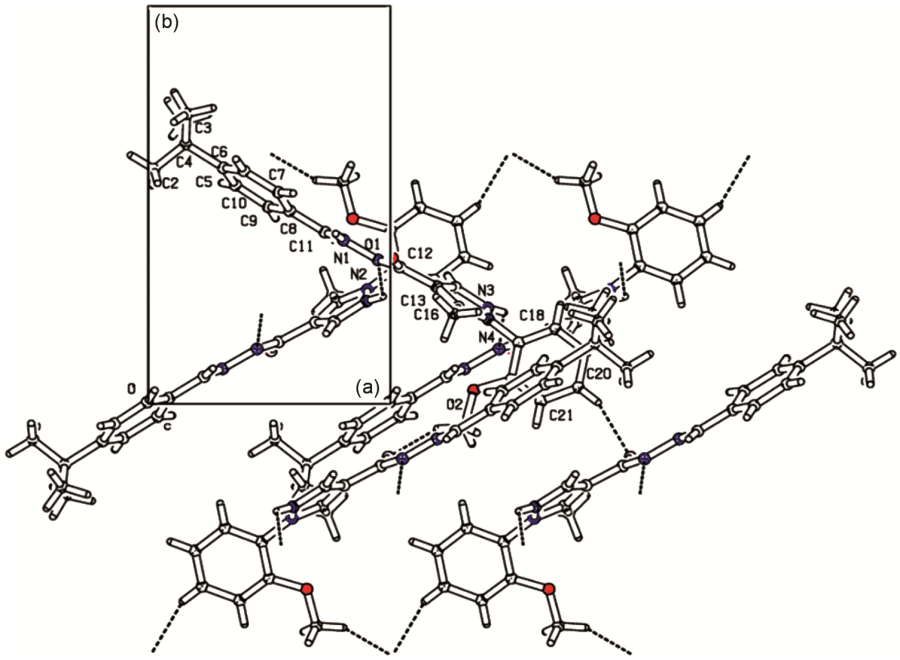

Fig. 6 — Package diagram of molecule **3**

Table 3 — Hydrogen bond geometry of (**3**) (Å, °)

D—H···*A*	*D*—H	H···*A*	*D*···*A*	*D*—H···*A*
C11—H11···N3^{i}	0.93	2.67	3.413 (11)	137
N2—H2···N3^{i}	1.00	2.18	3.101 (11)	152
C16—H16A···O2	0.96	2.65	3.228 (14)	119
C16—H16B···O1	0.96	2.42	3.099 (12)	127
C23—H23B···O1^{ii}	0.96	2.57	3.325 (14)	136

(i) *x*+1/2, −*y*+3/2, −*z*+1; (ii) −*x*+1, *y*+1/2, −*z*+3/2.

Table 4 — Geometric parameters of **3**

Parameter	XRD	DFT	HF
	Bond Lengths (Å)		
C1 - C4	1.481 (17)	1.549	1.542
C2 - C4	1.451 (16)	1.541	1.536
C3 - C4	1.521 (18)	1.549	1.542
C4 - C5	1.577 (13)	1.537	1.536
C5 - C10	1.358 (13)	1.410	1.417
C5 - C6	1.366 (13)	1.405	1.408
C6 - C7	1.431 (14)	1.392	1.394
C7 - C8	1.362 (13)	1.415	1.425
C8 - C9	1.385 (13)	1.416	1.427
C8 - C11	1.457 (12)	1.435	1.40
C9 - C10	1.384 (13)	1.387	1.385
C11 - N1	1.264 (11)	1.322	1.376
C12 - O1	1.202 (10)	1.256	1.247
C12 - N2	1.360 (11)	1.358	1.287
C12 - C13	1.517 (12)	1.482	1.505
C13 - C14	1.371 (11)	1.382	1.380
C13 - C15	1.400 (12)	1.411	1.392

(*Contd*.)

Table 4 — Geometric parameters of **3** (*Contd*.)

Bond Lengths (Å)

Parameter	XRD	DFT	HF
C14 - N3	1.356 (11)	1.373	1.323
C15 - N4	1.370 (11)	1.407	1.341
C15 - C16	1.465 (12)	1.486	1.494
C17 - C18	1.377 (12)	1.401	1.382
C17 - C22	1.393 (14)	1.417	1.399
C17 - N4	1.447 (11)	1.418	1.424
C18 - C19	1.406 (14)	1.396	1.386
C19 - C20	1.365 (16)	1.394	1.384
C20 - C21	1.402 (17)	1.401	1.388
C21 - C22	1.393 (14)	1.398	1.389
C22 - O2	1.377 (11)	1.362	1.334
C23 - O2	1.435 (14)	1.424	1.410
N1 - N2	1.416 (9)	1.351	1.392
N3 - N4	1.335 (9)	1.407	1.348
RMSE		0.039	0.042

Bond Angles (°)

Parameter	XRD	DFT	HF
C2 - C4 - C1	113.9 (13)	108.09	107.83
C2 - C4 - C3	112.5 (13)	108.05	107.83
C1 - C4 - C3	100.8 (13)	109.17	109.22
C2 - C4 - C5	107.5 (9)	112.40	112.33
C1 - C4 - C5	110.8 (9)	109.45	109.78
C3 - C4 - C5	111.4 (9)	109.59	109.75
C10 - C5 - C6	119.1 (9)	116.54	116.45
C10 - C5 - C4	120.8 (9)	120.21	120.06
C6 - C5 - C4	120.1 (9)	123.24	123.48
C5 - C6 - C7	119.3 (10)	122.19	122.19
C8 - C7 - C6	121.6 (9)	121.06	121.49
C7 - C8 - C9	117.2 (9)	116.82	116.02
C7 - C8 - C11	123.0 (9)	124.47	123.65
C9 - C8 - C11	119.6 (9)	118.69	120.32
C10 - C9 - C8	121.3 (10)	121.41	121.71
C5 - C10 - C9	121.4 (10)	121.94	122.10
N1 - C11 - C8	122.0 (9)	124.74	124.46
O1 - C12 - N2	125.5 (8)	125.20	130.46
O1 - C12 - C13	122.4 (8)	121.60	117.81
N2 - C12 - C13	112.1 (8)	113.18	111.72
C14 - C13 - C15	107.2 (8)	107.76	105.28
C14 - C13 - C12	129.0 (8)	124.04	126.31
C15 - C13 - C12	123.8 (8)	128.17	128.39
N3 - C14 - C13	110.3 (8)	109.17	109.02
N4 - C15 - C13	104.1 (7)	107.05	108.22
N4 - C15 - C16	123.4 (8)	122.08	121.66
C13 - C15 - C16	132.5 (8)	130.78	130.11
C18 - C17 - C22	121.0 (9)	119.49	121.13
C18 - C17 - N4	119.4 (9)	120.77	119.89
C22 - C17 - N4	119.3 (8)	119.62	118.97
C17 - C18 - C19	119.8 (10)	120.80	120.16

(*Contd*.)

Table 4 — Geometric parameters of **3** (*Contd*.)

Bond Lengths (Å)			
Parameter	XRD	DFT	HF
C20 - C19 - C18	120.1 (10)	119.57	118.85
C19 - C20 - C21	119.6 (11)	120.37	121.47
C22 - C21 - C20	121.0 (11)	120.43	119.80
O2 - C22 - C17	116.1 (9)	116.32	116.26
O2 - C22 - C21	125.5 (10)	124.36	125.16
C17 - C22 - C21	118.2 (9)	119.29	118.56
C11 - N1 - N2	117.5 (8)	124.21	115.40
C12 - N2 - N1	118.8 (8)	109.47	112.88
N4 - N3 - C14	105.3 (7)	107.80	109.12
N3 - N4 - C15	113.0 (7)	107.23	108.31
N3 - N4 - C17	121.3 (7)	117.14	120.90
C15 - N4 - C17	125.7 (7)	128.33	130.28
C22 - O2 - C23	118.1 (9)	118.74	120.54
RMSE		3.12	2.94
Torsion Angles (°)			
Parameter	XRD	DFT	HF
C2 - C4 - C5 - C10	83.2 (15)	179.4848	–179.9884
C1 - C4 - C5 - C10	−41.8 (15)	–60.3911	–60.0046
C3 - C4 - C5 - C10	−153.2 (13)	59.3093	60.062
C2 - C4 - C5 - C6	−96.9 (14)	–0.7295	–0.2074
C1 - C4 - C5 - C6	138.2 (12)	119.3946	119.7764
C3 - C4 - C5 - C6	26.8 (15)	–120.905	–120.157
C10 - C5 - C6 - C7	0.6 (16)	0.1091	–0.2704
C4 - C5 - C6 - C7	−179.4 (9)	–179.6838	179.9413
C5 - C6 - C7 - C8	−3.1 (17)	–0.053	–0.1858
C6 - C7 - C8 - C9	3.6 (16)	–0.0571	0.5755
C6 - C7 - C8 - C11	178.7 (10)	179.816	–179.0554
C7 - C8 - C9 - C10	−1.8 (17)	0.1087	–0.529
C11 - C8 - C9 - C10	−177.1 (10)	–179.772	179.1151
C6 - C5 - C10 - C9	1.2 (18)	–0.0568	0.3186
C4 - C5 - C10 - C9	−178.9 (10)	179.7429	–179.8854
C8 - C9 - C10 - C5	−0.6 (19)	–0.0526	0.0891
C7 - C8 - C11 - N1	12.8 (14)	–0.1526	–0.8853
C9 - C8 - C11 - N1	−172.3 (10)	179.7183	179.499
O1 - C12 - C13 - C14	−155.1 (10)	–178.5333	–177.7692
N2 - C12 - C13 - C14	22.0 (13)	1.5685	2.3003
O1 - C12 - C13 - C15	23.5 (14)	–0.2737	2.0752
N2 - C12 - C13 - C15	−159.5 (8)	179.8281	–177.8554
C15 - C13 - C14 - N3	1.2 (11)	–3.1791	–0.0687
C12 - C13 - C14 - N3	179.9 (8)	175.3844	179.8048
C14 - C13 - C15 - N4	−1.3 (10)	–3.1746	0.8321
C12 - C13 - C15 - N4	179.8 (8)	178.3396	–179.0378
C14 - C13 - C15 - C16	176.5 (11)	173.6139	–178.7513
C12 - C13 - C15 - C16	−2.3 (16)	–4.8719	1.3788
C22 - C17 - C18 - C19	−3.2 (14)	–0.8342	0.0289
N4 - C17 - C18 - C19	−177.8 (8)	–176.9924	179.8608
C17 - C18 - C19 - C20	−0.3 (15)	–0.6281	–0.0466
C18 - C19 - C20 - C21	1.1 (17)	1.0276	0.0681

(*Contd*.)

Table 4 — Geometric parameters of **3** (*Contd.*)

Bond Lengths (Å)			
Parameter	XRD	DFT	HF
C19 - C20 - C21 - C22	1.5 (17)	0.0517	–0.0709
C18 - C17 - C22 - O2	−178.9 (8)	–176.9481	–179.8359
N4 - C17 - C22 - O2	−4.2 (13)	–0.7454	0.3307
C18 - C17 - C22 - C21	5.6 (14)	1.8933	–0.0306
N4 - C17 - C22 - C21	−179.7 (8)	178.0961	–179.864
C20 - C21 - C22 - O2	−179.8 (10)	177.2299	179.8371
C20 - C21 - C22 - C17	−4.8 (15)	–1.5121	0.0506
C8 - C11 - N1 - N2	−178.1 (7)	–179.4266	171.9851
O1 - C12 - N2 - N1	0.4 (14)	0.4468	2.2384
C13 - C12 - N2 - N1	−176.6 (7)	–179.6593	–177.8423
C11 - N1 - N2 - C12	176.4 (8)	–179.7433	–154.019
C13 - C14 - N3 - N4	−0.5 (10)	8.3031	–0.7201
C14 - N3 - N4 - C15	−0.4 (9)	–10.1635	1.2539
C14 - N3 - N4 - C17	179.2 (8)	–162.9132	174.0712
C13 - C15 - N4 - N3	1.1 (10)	8.1471	–1.2834
C16 - C15 - N4 - N3	−177.0 (9)	–168.9831	178.3423
C13 - C15 - N4 - C17	−178.5 (8)	156.8515	–173.1988
C16 - C15 - N4 - C17	3.4 (14)	–20.2787	6.4269
C18 - C17 - N4 - N3	66.3 (11)	36.3548	94.7068
C22 - C17 - N4 - N3	−108.4 (10)	–139.7982	–85.4577
C18 - C17 - N4 - C15	−114.1 (10)	–109.7588	–94.2452
C22 - C17 - N4 - C15	71.2 (12)	74.0881	85.5903
C17 - C22 - O2 - C23	−174.7 (10)	178.5548	–176.7653
C21 - C22 - O2 - C23	0.4 (16)	–0.2211	3.4439

insight into the theoretical underpinnings of compound (3).

The expanded analytical spectrum, MEP, and FMO analyses were meticulously performed, harnessing the computational prowess of the DFT/B3LYP method in conjunction with the 6-31G+(d,p) basis set. Additionally, Hirschfeld surface analysis, a powerful tool for elucidating intermolecular interactions, was undertaken through the sophisticated Crystal Explorer 21.5 program[19]. These multifaceted analyses collectively contribute to a profound understanding of the electronic and structural facets inherent in compound (3) at a theoretical level, enriching the depth of our exploration.

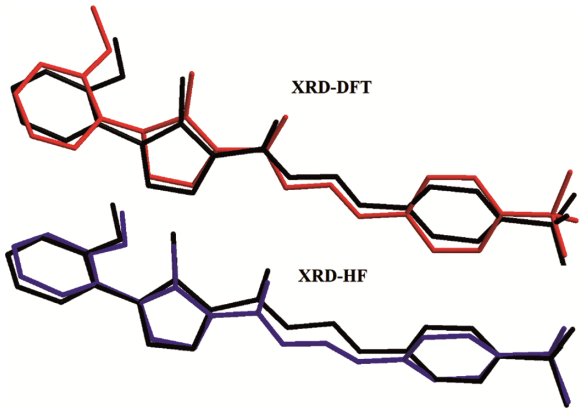

Fig. 7 — The optimized geometries of (3) obtained by experimental and theoretical methods are shown in the XRD - black, HF blue, and DFT red overlaps

Optimization geometry

Molecular modeling endeavors routinely leverage the HF and DFT methods[20]. In the course of this investigation, we embarked on determining the minimum energy conformations of compound (3) through meticulous geometric optimization calculations. These involved the application of both HF and DFT/B3LYP methods, utilizing a 6-31G+(d,p) basis set to capture the molecular intricacies. The visual representation of the resultant minimum energy molecular conformation is encapsulated in Fig. 7, while a detailed exposition of the corresponding bond lengths, bond angles, and torsion angles is systematically presented in Table 4.

To rigorously gauge the precision of the calculated geometric parameters in comparison to experimental data, a thorough analysis of Root Mean Square Error

(RMSE) values was conducted, encompassing both maximum difference and mean error squares for bond lengths and bond angles. A judicious comparison of outcomes derived from the HF and B3LYP methods revealed a noteworthy distinction. Notably, the B3LYP method emerged as the more adept approach, demonstrating superior accuracy in faithfully representing the experimental geometry for both bond lengths and bond angles.

The presented RMSE values served as a metric for the root mean square error between experimental and calculated bond lengths and bond angles, using both DFT and HF methods. The DFT method yielded a smaller RMSE value (0.039Å) for bond length compared to the HF method (0.042Å), indicating greater accuracy in predicting bond lengths. Conversely, the HF method produced a smaller RMSE value (2.94°) for bond angles compared to the DFT method (3.12°), indicating its superior accuracy in predicting bond angles.

Recognizing the significance of lower Root Mean Square Error (RMSE) values as indicators of enhanced alignment between theory and experiment, it is imperative to underscore that the absolute magnitude of these values alone does not furnish a comprehensive gauge of the accuracy or reliability of the computational method. The precision of calculated results hinges on a multitude of factors, including the quality of the basis set, the selected function, and the inherent characteristics of the studied molecule, collectively shaping the overall fidelity of the outcomes[21].

Fundamentally, the HF method emerged as a robust tool for accurately predicting bond lengths, while the DFT method demonstrated superior proficiency in delineating bond angles and overall molecular geometry. Despite discernible disparities between experimental and theoretical outcomes, the DFT method persists as a suitable choice for forecasting the physical and chemical properties of the compound (**3**). An in-depth evaluation of the alignment between experimental and optimized geometries was conducted through molecule overlapping using the CHEM3D program[22]. Additionally, the DFT method was employed to conduct an energy analysis, delineating the minimum energy configuration of (**3**) by iteratively adjusting the torsion angle T(C7 - C8 - C11 - N1) in one of the aromatic rings in 5° increments from 0°/360°. Point energy was meticulously calculated at each angle value, as visually depicted in Fig. 8.

Fig. 8 illuminates the intricacies of the potential energy surface, unveiling two symmetrical potential barriers lying at angles of 90° and 270°. Notably, these angles correspond to the apex of the molecule's energy configuration, where the rings exhibit a perpendicular alignment. Conversely, the potential energy surface showcases four distinct minima around angles of 40°, 140°, 220°, and 350°, indicative of molecular stability at these specific angular positions.

Delving deeper into the molecular dynamics, the torsion angle analysis T(C7 - C8 - C11 - N1) yields compelling insights. Strikingly, both the X-ray and calculated values align harmoniously with the global

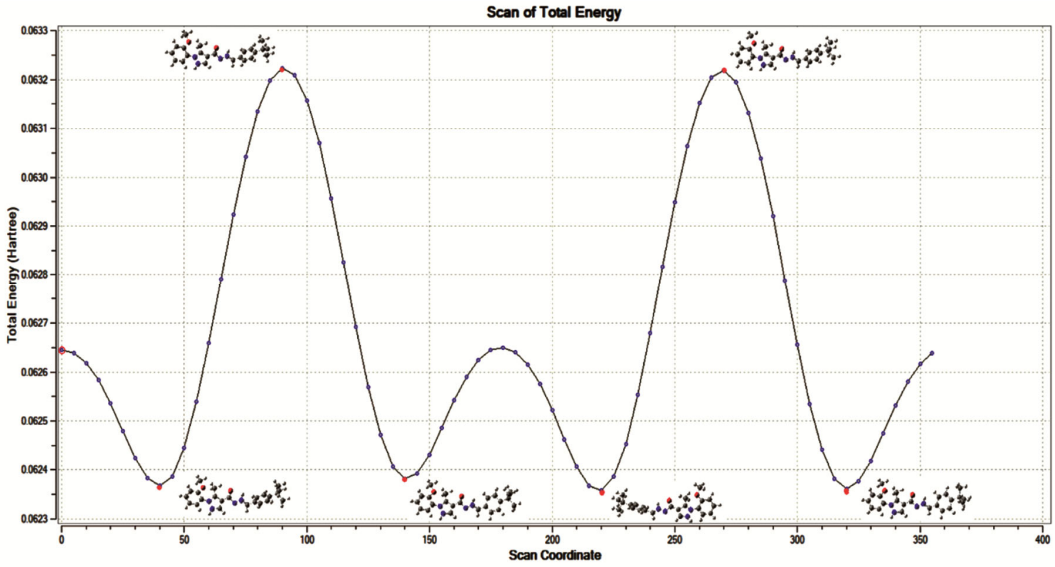

Fig. 8 — Energy change graph of (**3**) depending on torsion angle T(C7 - C8 - C11 - N1)

energy minimum, signifying not only the attainment of the lowest energy state through geometry optimization but also the establishment of the most stable molecular configuration. This alignment is robustly supported by the corroborative X-ray data presented in Table 4. The congruence between the calculated results and experimental observations underscores the reliability and precision of the geometry optimization approach, solidifying its efficacy in elucidating and characterizing the stable molecular configurations with a high degree of confidence.

HOMO-LUMO

The HOMO (highest occupied molecular orbital) and LUMO (lowest unoccupied molecular orbital) stand as pivotal orbitals governing the intricate dance of molecules during reaction mechanisms. In the symphony of chemical reactions, the HOMO energy denotes the orbital's propensity to relinquish electrons (π-donor), while the LUMO energy signifies its eagerness to embrace electrons (π-acceptor)[23]. The depictions of HOMO and LUMO for the scrutinized molecule were crafted through the precision of the B3LYP method and the 6-31G+(d,p) basis set. Refer to Fig. 9 for a visual representation of these intricate orbitals.

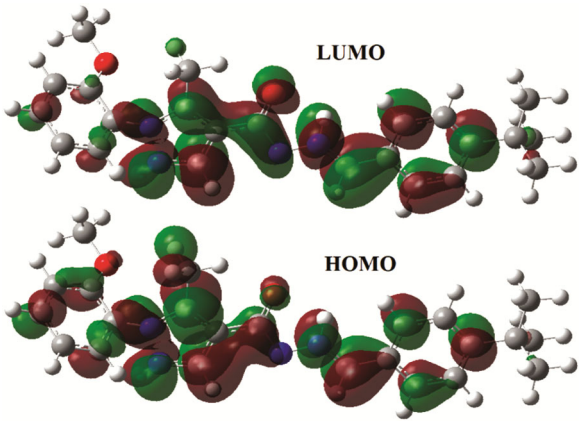

Fig. 9 — HOMO and LUMO configuration of **3**

The energy benchmarks for the HOMO and LUMO orbitals of compound (3) stand at -5.21 eV and -1.66 eV, respectively. This results in a nuanced energy delta of -3.55 eV between these orbitals, aligning harmoniously with values echoed in the literature for analogous compounds[24,25]. The energies of HOMO and LUMO bestow valuable insights into the molecule's disposition for electron contribution and acceptance, enriching our comprehension of its reactivity and potential engagement in chemical symphonies.

Molecular electrostatic potential (MEP)

Fig. 10 provides a comprehensive visualization of the MEP surface, a tool essential for understanding the electrostatic potential distribution across the molecule. This representation serves to elucidate the intricate charge distribution, offering valuable insights into potential electrophilic addition sites. Regions of negative charge are vividly represented in red, indicating locales where an electrophile is most likely to interact favorably.

Additionally, the ionization potential energy surface contributes profound insights into electrophilic interactions. Constructed by combining the energy required for electron removal with the electron density, this surface highlights areas, depicted in red, where electron removal occurs with minimal energy cost. A holistic examination of both the MEP and local ionization potential energy surfaces empowers researchers to decipher critical information regarding molecular charge distribution and to pinpoint sites predisposed to electrophilic interactions.

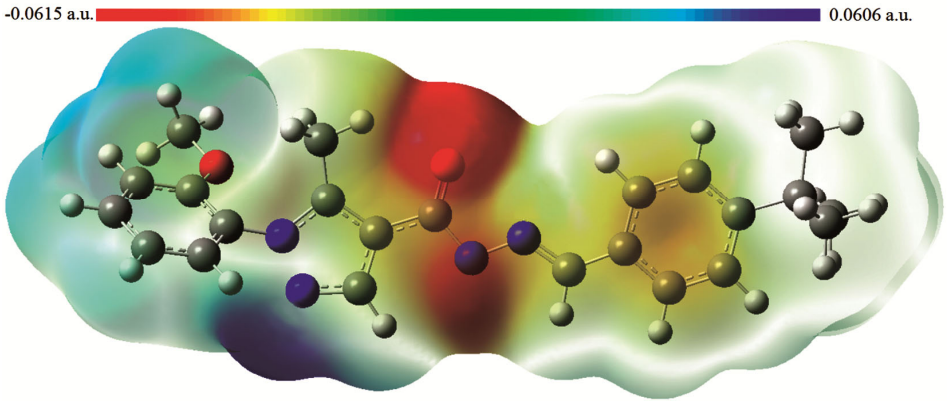

Fig. 10 — Calculated electrostatic potential surfaces on the molecular surfaces for **3**

The MEP surface stands out as a powerful predictive tool for discerning a molecule's reactivity toward electrophiles or nucleophiles, providing a visual representation of its electrostatic potential. Areas characterized by high electron density (negative potential) are particularly prone to nucleophilic attacks, whereas those with low electron density (positive potential) are predisposed to electrophilic attacks. The utilization of a color-coded MEP surface further enhances the distinction between positive and negative potential regions[26].

Upon conducting a meticulous analysis of the MEP map, a discernible spatial distribution is revealed. The red regions prominently concentrate around the oxygen atom, signifying areas highly receptive to nucleophilic interactions. In contrast, the maximum blue region is localized on hydrogen atoms bonded to nitrogen atoms, suggesting heightened susceptibility to electrophilic interactions. Specifically, on the MEP map, the O1 atom exhibits the most negative region with a value of -0.0615 atomic units, underscoring its significance in nucleophilic reactivity. Simultaneously, the nitrogen atom in the pyrazole ring displays the most positive region with an MEP value of 0.0606 atomic units, designating it as a key site for potential electrophilic reactions. These comprehensive findings strongly support the assertion that the O1 atom, due to its pronounced negative potential, stands as the most favorable locus for electrophilic reactions within the intricate molecular structure.

Thermodynamic properties

This statement delves into the standard thermodynamic functions, meticulously derived through vibrational analysis and statistical thermodynamics at the B3LYP/6-31G+(d,p) level. The exhaustive data, encapsulated in Table 5, meticulously outlines key thermodynamic parameters such as enthalpy ($H°_m$), heat capacity ($C°_{p,m}$), and entropy ($S°_m$).

Upon a thorough examination of the data within Table 5, a discernible pattern emerges a consistent upward trajectory in these thermodynamic functions across the temperature spectrum of 100.00 to 500.00 K. This ascending trend is elucidated as a direct consequence of the escalating intensity of molecular vibrations with rising temperatures. The inference drawn from this dataset is compelling: the compound in question exhibits a remarkable degree of thermal stability. Furthermore, it suggests that the compound's thermodynamic characteristics can be robustly extrapolated over a designated temperature range (100.00 to 500.00 K). This significant observation not only underscores the inherent stability of the compound but also positions it as a reliable candidate for a myriad of applications across a broad and dynamic temperature spectrum[27].

Table 5 — The standard thermodynamic functions

	Enthalpy ($H°_m$)	Heat Capacity ($C°_{p,m}$)	Entropy ($S°_m$)
100	2.364	38.528	104.518
200	8.096	71.624	142.937
293	16.353	102.098	176.473
300	17.090	104.398	178.958
400	29.331	135.885	213.954
500	44.516	163.009	247.726

A goodness of fit is a numerical metric that gauges the efficacy of a model in conforming to a given dataset. In the specific context of this study, a fit factor value of 0.999 or higher signifies an exceptional alignment of quadratic equations employed to establish correlation equations between thermodynamic properties and temperatures. This elevated level of goodness of fit suggests that the models not only effectively capture the intricate relationships inherent in the data but also enable accurate predictions of these thermodynamic properties across a spectrum of temperatures within the investigated range. In essence, the robust goodness of fit values underscores the reliability and precision of the models in encapsulating the complex interplay between thermodynamic properties and varying temperatures.

The correlation equations utilized for this purpose are as follows:

$$H_m^0 = -0{,}28976 + 0{,}01042T + 1{,}5853 \times 10^{-4}T^2, (R^2 = 0{,}99998)$$

$$C_{p,m}^0 = 2{,}2548 + 0{,}36831T - 0{,}91783 \times 10^{-4}T^2, (R^2 = 0{,}9997)$$

$$S_m^0 = 65{,}28887 + 0{,}40101T - 0{,}72612 \times 10^{-4}T^2, (R^2 = 0{,}99998)$$

Hirshfeld Surface Analysis

Hirshfeld analysis emerges as a formidable instrument for unraveling the intricate electronic interactions within the crystalline framework of a molecule, providing a profound understanding of electron distributions, molecular interplays, and crystal structures. In the context of this study, a meticulous Hirshfeld surface analysis was executed

using the CrystalExplorer 21.5 program, aiming to unveil the subtle intricacies of the crystal structure's interactions[20].

The vividly rendered 3D surfaces in Fig. 11, distinguished by vibrant red and blue hues, delineate the d_{norm}, d_e, and d_i surfaces. Noteworthy are the red dots embellishing the d_{norm} Hirshfeld surface, serving as markers for robust hydrogen bonds, with darker red dots indicating higher bond strengths. Specifically, the hydrogen bonds meticulously identified in Table 3 (N2-H3---N3, C11-H11---N3, and C23-H23B---O1), are unequivocally substantiated by the discernible presence of dark red dots on the d_{norm} Hirshfeld surface.

This correlation not only fortifies the reliability of the identified hydrogen bonds but also attests to the remarkable capability of Hirshfeld analysis in unveiling the nuanced intricacies of crystal structures and their associated interactions. The insights garnered through this comprehensive analytical approach contribute significantly to our in-depth comprehension of the molecular architecture and intermolecular forces governing the crystal lattice.

Fig. 12 shows regions indicating the percentages of different interactions (H----H, C---H, O---H, N---H and C---C) within the structure. The highest interaction sites were observed in H----H interactions (60.8%), followed by C---H (21.5%), O---H (8.6%), N---H (7.1%) and C---C (1.3%). The fingerprint region depicted in Fig. 13 serves as a comprehensive visual synthesis encapsulating all discernible interactions. Notably, our observation reveals a striking concordance between the interactions identified in the Hirshfeld surface analysis of

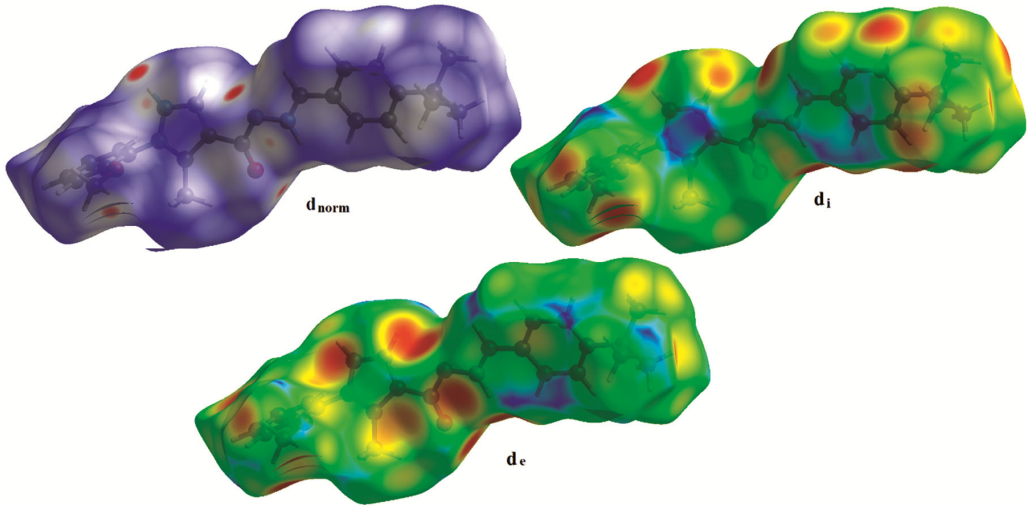

Fig. 11 — d_{norm}, d_e and d_i Hirshfeld surface of **3**

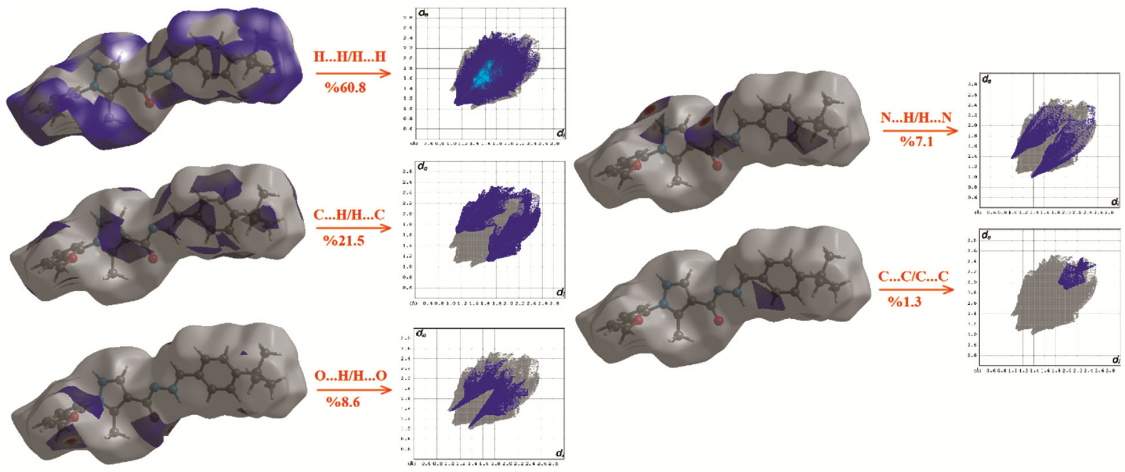

Fig. 12 — Interactions that contribute to the total Hirshfeld surface for **3**

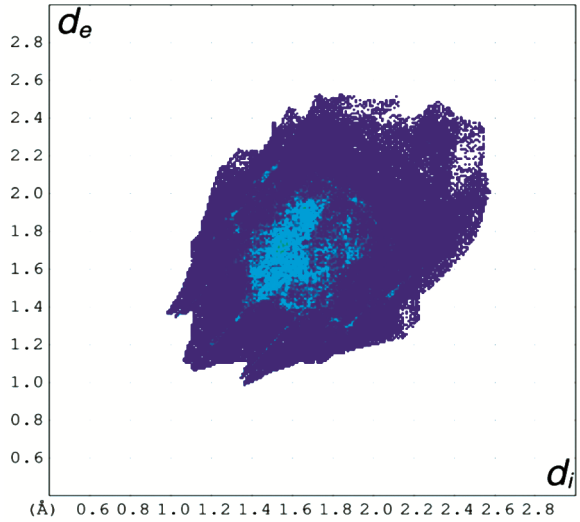

Fig. 13 — 2D fingerprint representation of **3**

Table 6 — The calculated dipole moment μ_{tot} (Debye), the average polarizability α_{tot} (Å^3), and the first hyperpolarizability β_{tot} ($\times10^{-30}$ cm^5/esu) for the title compound.

μ_x	–4.9976	β_{xxx}	–4815.1425
μ_y	–1.0348	β_{xxy}	–6078.3678
μ_z	–1.6709	β_{xyy}	–950.1518
μ_{tot}	5.3702	β_{yyy}	–317.0890
α_{xx}	1888.9873	β_{xxz}	1999.5777
α_{xy}	36.8052	β_{xyz}	–413.8162
α_{yy}	296.3471	β_{yyz}	–42.4691
α_{xz}	–32.8534	β_{xzz}	–951.3819
α_{yz}	11.1064	β_{yzz}	–201.4410
α_{zz}	223.6617	β_{zzz}	4.0944
α_{tot}	119.004	β_{tot}	83.0807×10^{-30}

compound (3) and those observed in analogous structures studied previously[28-30].

NLO

The intricate field of Nonlinear Optics (NLO) analysis delves deep into the examination of a molecule or material's response under the influence of high-intensity light, specifically focusing on its ability to generate NLO effects. This comprehensive analysis serves as a cornerstone for unraveling the nuanced NLO properties intrinsic to the material, ultimately facilitating the tailored design and development of new materials endowed with distinctive NLO characteristics. These advancements, in turn, play a pivotal role in driving diverse technological breakthroughs[31,32].

NLO effects, a consequence of the interaction between electromagnetic fields and various media, give rise to the generation of new fields characterized by alterations in phase, frequency, amplitude, or other transmission characteristics in comparison to interfering fields[33]. The ongoing research in nonlinear optics is a driving force behind material and technological advancements, finding widespread applications within the expansive realm of photonics[30].

The computed total dipole moment for compound (**3**) stands impressively at 5.3702 D, accompanied by a calculated polarization (αtot) of 119.004 Å^3. The nuanced polarization (αij) values, as detailed in Table 6, prominently feature non-zero values, with a notable dominance of diagonal components.

Noteworthy is the determination of the total first hyperpolarization (βtot) for compound (**3**) at 83.0807×10^{-30} cm^5/esu, a value significantly surpassing the urea value obtained *via* the B3LYP/6-31+G(d) method (βtot value 0.77×10^{-30} cm^5/esu). Particularly striking is the theoretical prediction that the first hyperpolarization of the title compound is 107.9 times larger than that of urea. These compelling results unequivocally demonstrate that the compound exhibits a remarkably enhanced first hyperpolarization property compared to urea, positioning it as a promising candidate for advanced applications in nonlinear optics[34].

Conclusions

In the pursuit of advancing our understanding, a hydrazone derivative was meticulously synthesized *via* a condensation reaction and subjected to a comprehensive array of analytical techniques, including X-ray diffraction (XRD) and infrared spectroscopy (FTIR). The XRD analysis not only affirmed the stability of the compound's crystal structure but also classified it within the orthorhombic $P2_12_12_1$ space group. Augmenting this, FMO calculations provided additional insights, reinforcing the inherent stability of the synthesized compound.

Beyond structural elucidation, Hirshfeld surface analysis was employed to unravel the intricacies of binding and interaction patterns within the molecular framework. This holistic approach aimed to provide a nuanced perspective on the compound's intermolecular relationships.

The research horizon further expanded to predicting correlations between essential thermodynamic properties ($H°_m$, $C°_{p,m}$, $S°_m$) and varying temperatures (T). Theoretical calculations, executed through diverse methods, harmonized seamlessly with the XRD results, affirming the precision of our computational models.

Crucially, the synthesized hydrazone derivative emerges as a compelling candidate for industrial applications, with its performance attributes aligning with the demands of industrial studies. The congruence between experimental and theoretical findings not only underscores the reliability of the structural characteristics but also positions the synthesized compound as a promising player in diverse industrial contexts. This realization prompts an enduring journey of exploration and investigation, as we navigate the rich potential this compound holds for future industrial endeavors.

Remarkably, the synthesized compound showcased superior NLO properties in comparison to urea, positioning it as a highly promising candidate for second-order NLO materials. This breakthrough not only signifies a significant advancement in the realm of nonlinear optics but also makes a noteworthy contribution to the broader landscape of material design and synthesis. The compound's enhanced NLO properties open up exciting avenues for the development of novel materials with enhanced functionalities, holding great potential for applications in various technological domains.

Supplementary Information

CCDC 2321709 contain the supplementary crystallographic data for this paper. This data can be obtained free of charge from The Cambridge Crystallographic Data Centre *via* www.ccdc.cam.ac.uk/data_request/cif. For the decimal rounding of numerical parameters and su values, the rules of IUCr have been employed[35].

References

1 Rubanov Z M, Levin V V & Dilman A D, *Adv Syn Catal*, 365 (2023) 2636.
2 Lygaitis R, Getautis V & Grazulevicius J V, *Chem Soc Rev*, 37 (2008) 770.
3 Belyaeva E R & Ishmuratov Y G, *Russian J Gen Chem*, 93 (2023) 124.
4 Su X & Aprahamian I, *Chem Soc Rev*, 43 (2014) 1963.
5 El-Nagar I, Youssef A M, El-Hakim A A A, Kenawy E-R, Mandour H S A & Khattab T A, *Chemosensors*, 10 (2022) 451.
6 Zheng H W, Yang D D, Shi Y S, Xiao T, Tan H W & Zheng X J, *Inorg Chem*, 62 (2023) 6323.
7 Men G & Lehn J M, *Chem Sci*, 10 (2018) 90.
8 Sarigöl D, Yüksel D, Okay G & Uzgören-Baran A, *J Mol Struc*, 1086 (2015) 146.
9 Sheldrick G M, *Acta Cryst*, A64 (2008) 112.
10 Sheldrick G M, *Acta Cryst*, C71 (2015) 3.
11 Farrugia L J, *J Appl Cryst*, 45 (2012) 849.
12 Spek A L, *Acta Cryst*, D65 (2009) 148.
13 Thomas K D, Adhikari A V, Telkar S, Chowdhury I H, Mahmood R, Pal N K, Row G & Sumesh E, *Eur J Med Chem*, 46 (2011) 5283.
14 Kassab R M, Gomha S M, Al-Hussain S A, Dena A S A, Abdel-Aziz M M, Zaki M E A & Muhammad Z A, *Arabian J Chem*, 14 (2021) 103396.
15 Younis A M, Rakhaa T H, El-Gamil M M & El-Reash G M A, *J Mol Struc*, 1245 (2021) 131110.
16 Martínez R F, Avalos M, Babiano R, Cintas P, Light M E, Jimenez J L & Rastrojo V, *Tetrahedron*, 67 (2011) 2025.
17 Frisch M J, Trucks G W, Schlegel H B, Scuseria G E, Robb M A, Cheeseman J R, Scalmani G, Barone V, Mennuci B, Petesson G A, Nakatsuji H, Caricato M, Li X, Hratchian H P, Izmaylov A F, Bloino J, Zheng G, Sonnenberg J L, Hada M, Ehara M, Toyota K, Fukuda R, Hasegawa J, Ishida M, Nakajima T, Honda Y, Kitao O, Nakai H, Vreven T, Montgomery J, Peralta J E, Ogliaro F, Bearpark M, heyd J J, Brothers E, Kudin K N, Staroverov V N, Kobayashi R, Normand J, Raghavachari K, Rendell A P, Burant J C, Iyengar S S, Tomasi J, Cossi M, Rega N, Millam J M, Klene M, Knox J E, Cross J B, Bakken V, Adamo C, Jaramillo J, Gomperts R, Stratmann R E, Yazyev O, Austin A J, Cammi R, Pomelli C S, Ochterski J W, Martin R L, Morokuma K, Zakrzewski V G, Voth G A, Salvador P, Dannenberg J J, Dapprich S, Daniels A D, Farkas O, Foresman J, Ortiz J V, Cioslowski J & Fox D J, *Gaussian 03, Revision E.01*, (Gaussian, Wallingford, Conn, USA), 2004.
18 Dennington R, Keith T & Millam J, *GaussView, Version 4.1*, (Semichem, Shawnee Mission, Kan, USA), 2007.
19 Spackman P R, Turner M J, McKinnon J J, Wolff S K, Grimwood D J, Jayatilaka D & Spackman M A, *J Appl Cryst*, 54 (2021) 1006.
20 Khan S A, Adhikari A, Ayub K, Farooq A, Mahar S, Qureshi M N & Mahmood T,. *Spectrochim Acta Part A: Mol Biomol Spect*, 217 (2019) 113.
21 Lewars E G, *Computational Chemistry: Introduction to the Theory and Applications of Molecular and Quantum Mechanics*, (Springer Science & Business Media) 2003, p. 385.
22 Chem Office protocol; 2017. Available from: http://www.cambridgesoft.com/Ensemble_for_Chemistry/details/Default.aspx?fid=16andpid=735. (Reference not found kindly provide a valid URL Link)
23 Tanak H, *J Phys Chem A*, 115 (2011) 13865.
24 González-Baró A C, Pis-Diez R, Parajón-Costa B S & Rey N A, *J Mol Struc*, 1007 (2012) 95.
25 Bülbül H, Köysal Y, Yıldırım S Ö, Ünlüer D, Soylu M S & Butcher R J, *J Chem Cryst*, 52 (2022) 440.
26 Santiago P H, Tiago F S, Castro M S, Souza P E, Martins J B & Gatto C C, *J Inorg Biochem*, 204 (2020) 110949.
27 Bülbül H, Atalay Ş & Ertürk A G, *J Mol Struc*, 1291 (2023)136002.
28 Al - Karawi A J M, Ali A-M B O, Dege N & Kansız S, *Chem Papers*, 75 (2021) 3901.
29 Mohamadi M, Ebrahimipour S Y, Castro J & Foro S, *J Mol Struc*, 1299 (2024) 137057.

30 Bülbül H, Çetin G, Köysal Y, Şimşek R, Öztürk Y S, Tanak H & Butcher R J, *Mol Phys*,122 (2024) e2320784.
31 Tanak H, Köysal Y, Isık S, Yaman H & Ahsen V, *Bull Korean Chem Soc*, 32 (2011) 673.
32 Andraud C, Brotin T, Garcia C, Pelle F, Goldner P, Bigot B & Collet A, *J Am Chem Soc*, 116 (1994) 2094.
33 Bülbül H, Atalay Ş & Ertürk A G, *Indian J Chem*, 62(2023) 1091.
34 Groom C R, Bruno I J, Lightfoot M P & Ward S C, *Acta Cryst*, B72 (2016) 171.
35 Clegg W, *Acta Cryst*, E59 (2003) e2-e5.